Entropy-stabilized Isolated Active Pd Species within High-entropy Fluorite Oxide Matrix for CO_2 Hydrogenation to Formic Acid

Kohsuke Mori,[*ab] Yuki Shimada,[a] Hideto Yoshida,[c] Yoyo Hinuma,[d] and Hiromi Yamashita[ab]

[a] Division of Materials and Manufacturing Science, Graduate School of Engineering, Osaka University, 2-1 Yamada-oka, Osaka 565-0871, Japan.

E-mail: mori@mat.eng.osaka-u.ac.jp

[b] Innovative Catalysis Science Division, Institute for Open and Transdisciplinary Research Initiatives (ICS-OTRI), Osaka University, Suita, Osaka 565-0871, Japan.

[c] SANKEN, Osaka University, 8-1Mihogaoka, Ibaraki, Osaka 567-0047, Japan.

[d] Department of Energy and Environment, National Institute of Advanced Industrial Science and Technology (AIST), 1-8-31, Midorigaoka, Ikeda, Osaka 563-8577, Japan

Abstract:

Active, stable Pd species were incorporated within the matrix of the fluorite-based high-entropy oxide (HEO) $(YZrLaGdHf)_xO_2$ using an entropy-driven strategy based on a liquid-phase reaction. In situ X-ray absorption fine structure analyses and transmission electron microscopy observations at elevated temperatures under H_2 confirmed that partially aggregated Pd oxide species in the as-synthesized Pd@$(YZrLaGdHf)_xO_2$) were transformed into an entropy-stabilized isolated form at 600 °C. In contrast, Pd species on the $(YZrLaGdHf)_xO_2$ surface were readily reduced with the formation of nanoclusters/nanoparticles even in the temperature range of 100 to 200 °C. This HEO incorporating Pd exhibited enhanced activity during the hydrogenation of CO_2 to formic acid with a maximum turnover number of 5000 based on the quantity of surface-exposed Pd atoms. This performance was more than eight times higher than that of the Pd/$(YZrLaGdHf)_xO_2$ on the basis of supported Pd. An assessment of kinetics and theoretical investigations suggested that entropy-stabilized isolated Pd species facilitated both H_2 dissociation and the attack of dissociated H atoms on C atoms in HCO_3^- ions.

KEYWORDS: High-entropy oxides • Palladium • Catalyst • Formic acid • Carbon dioxide

1. Introduction

Multicomponent solid solutions have attracted significant attention as so-called high-entropy materials exhibiting fascinating properties derived from high values of configurational entropy (ΔS_{conf}).[1-4] In 2005, Rost et al. suggested the concept of high entropy oxides (HEOs) as a new class of single-phase materials composed of five or more metal oxides and having random occupancies.[5] Subsequently, HEOs with various crystal structures, such as rock salt-type, perovskite-type oxides, spinel-type, and fluorite-type oxides, were developed.[6] The wide range of possible HEO compositions suggests many potential applications, including in batteries and catalysis.[7-9] In particular, the high ΔS_{conf} values of such materials that result from the large number of components is a prominent characteristic. According to the Gibbs free energy equation $G = H - TS$, (where G is the Gibbs free energy, H is the enthalpy, T is the temperature and S is the entropy), phase stability will be principally determined by competing enthalpic and entropic effects. Specifically, higher temperatures and higher ΔS_{conf} values will stabilize a given system by lowering the overall G value. HEOs in particular are able to stabilize foreign atoms based on a pronounced entropy effect at high temperatures, depending on the combination of constituent elements that is employed.[10-14] For example, entropy-driven stabilization of single-atom Pd within $(CeZrHfTiLa)O_x$ has been established by a mechanical milling followed by the calcination at 900 ºC, which shows outstanding low-temperature CO oxidation activity as well as high resistance toward thermal and hydrothermal degradation.[10] More recently, the crucial role of oxygen vacancies in HEOs is also well investigated. This research demonstrated that the higher amount of oxygen vacancies promotes the surface oxygen exchange, which facilitates the efficient N_2 dissociation and thus leads to higher NH_3 formation yield.[15]

The hydrogenation of CO_2 to produce formic acid (FA; HCOOH) is an important reaction because FA has a relatively high hydrogen content (53 g L^{-1}), is nonflammable under ambient conditions, and exhibits low toxicity.[16-18] This compound is also being considered as a renewable hydrogen storage material in CO_2-mediated energy cycles because FA can efficiently release hydrogen and CO_2 in the presence of appropriate catalysts. The synthesis of FA via CO_2 hydrogenation is typically performed in the liquid phase in the presence of a weak base (B) that shifts the thermodynamic equilibrium to the product side based on the equation CO_2 (aq) + H_2 (aq) + B $\rightarrow$ HCO_2^- (aq) + BH^+, $\Delta G = -35.4$ kJ·mol^{-1}.[19] However, reliable heterogeneous catalysts for this reaction have not yet been developed in spite of the practical advantages such materials would provide.[20-21] The fabrication of precious metal catalysts that are not prone to sintering would be especially desirable because supported active metal nanoparticles tend to agglomerate at high temperatures, drastically reducing the catalytic performance. Such agglomeration can be inhibited by utilizing the strong interactions between metal nanoparticles and catalyst supports, which can also generate unique synergistic effects at the interfaces between these materials.[22] In addition, the surface modification

of support materials with organic ligands can inhibit the aggregation of metal nanoparticles through specific metal-ligand electronic effects.[23]

The present study incorporated active Pd species within the HEO $(YZrLaGdHf)_xO_2$, which is the typical single-phase multi-component fluorite-type oxides. It was anticipated that the high-entropy effects originating from the number of components in this HEO matrix would solve the aggregation problem of supported metals. As expected, entropy-stabilized isolated Pd species were obtained, as evidenced by in situ observations at elevated temperatures under H_2. Enhanced catalytic activity during the hydrogenation of CO_2 to generate FA was also observed.

2. Experimental

2.1. Materials: Na_2PdCl_4 was obtained from the Tokyo Kasei Kogyo Co., Ltd. while $La(NO_3)_3·6H_2O$), $Ce(NO_3)_3·6H_2O$, $HfCl_4$, $Gd(NO_3)_3·5H_2O$, $ZrO(NO_3)_2$, $NH_4)_2[TiO(C_2O_4)_2]·nH_2O$ and hexamethylene tetramine were purchased from Nacalai Tesque. Poly(ethylene glycol)-block-poly(propylene glycol)-block-poly(ethylene glycol) [P123] and $Y(NO_3)_3·6H_2O$ were purchased from Sigma-Aldrich. All commercially available compounds were used as received. Distilled water was employed as the reaction solvent.

2.2. Synthesis of Pd@$(YZrLaGdHf)_xO_2$

$Y(NO_3)_3·6H_2O$ (0.5744 g), $ZrO(NO_3)_2·2H_2O$ (0.4009 g), $La(NO_3)_3·5H_2O$ (0.6495 g), $Gd(NO_3)_3·5H_2O$ (0.6500 g), $HfCl_4$ (0.4805 g) and 37.5 mL of distilled water were combined in a 500 mL flask and the mixture was ultrasonicated until all reagents were completely dissolved. Following this, a solution of 3.0 g of P123 in 56 mL of ethanol was added after which ethylene glycol (180 mL), hexamethylenetetramine (1.05 g) and Na_2PdCl_4 (0.0784 g) were added and the mixture was stirred for 45 min. The resulting solution was transferred into an autoclave with a Teflon liner and heated at 170 °C for 15 h, followed by cooling. The solid product was recovered, washed with ethanol and water, and dried overnight under vacuum. Finally, the product was ground in an agate mortar and calcined in air at 400, 600 or 800 °C for 2 h to obtain the Pd@$(YZrLaGdHf)_xO_2$. The Pd@$(TZrLaCeHf)_xO_2$ was prepared by the same procedure but using $(NH_4)_2[TiO(C_2O_4)_2]·3H_2O$ (0.4948 g) and $Ce(NO_3)_3·6H_2O$ (0.6513 g).

2.3. Synthesis of Pd/$(YZrLaGdHf)_xO_2$

$Y(NO_3)_3·6H_2O$ (0.5744 g), $ZrO(NO_3)_2·2H_2O$ (0.4009 g), $La(NO_3)_3·5H_2O$ (0.6495 g), $Gd(NO_3)_3·5H_2O$ (0.6500 g), $HfCl_4$ (0.4805 g) and 37.5 mL of distilled water were combined in a 500 mL flask and ultrasonicated until the reagents were completely dissolved. Following this, a solution of 3.0 g of P123 in 56 mL of ethanol was added to the precursor mixture. Ethylene glycol (180 mL) and hexamethylenetetramine (1.05 g) were subsequently added and the mixture stirred for 45 min. The resulting

solution was transferred into an autoclave with a Teflon liner and heated at 170 °C for 15 h, followed by cooling. The product was then separated, washed with ethanol and water, and dried overnight under vacuum. Finally, the mixture was ground in an agate mortar and calcined in air at 800 °C for 2 h to obtain the $(YZrLaGdHf)_xO_2$.

A 0.5 g quantity of this material was dispersed in a mixture of 100 mL of an aqueous solution containing Na_2PdCl_4 (0.0142 g), then the mixture was stirred at room temperature for 1h. The suspension was evaporated under vacuum, and the obtained powder was dried overnight. Subsequently, the sample was reduced with H_2 (20 mL/min, 400 °C) for 2 h to yield the $Pd/(YZrLaGdHf)_xO_2$ having a Pd content of 1.0 wt%. $Pd/(TiZrLaCeHf)_xO_2$ was prepared by the same procedure but using $(NH_4)_2[TiO(C_2O_4)_2]\cdot 3H_2O$ (0.4948 g) and $Ce(NO_3)_3\cdot 6H_2O$ (0.6513 g). ICP analysis clearly indicated that the desired amounts of metal species were successfully loaded onto each support

2.4. General procedure for the catalytic hydrogenation of CO_2: CO_2 hydrogenation to FA was conducted with a batch reactor system using a stainless-steel autoclave (60 mL). In each trial, a portion of the catalyst (30 mg) and a 1.0 M aqueous $NaHCO_3$ solution (10 mL) were transferred into the reactor after which the pressure in the device was increased to 2.0 MPa by adding H_2 and CO_2 in a 1:1 molar ratio. The system was subsequently heated to 100 °C and stirred for 24 h. FA yields were determined based on analyses by high-performance liquid chromatography at 40 °C using a Shimadzu instrument equipped with a Bio-Rad Aminex HPX-87H ion exclusion column (300 × 7.8 mm) with 5 mM H_2SO_4 at a flow rate of 0.5 mL/min as the mobile phase. TON values were determined by dividing the quantity of FA produced after 6 h by the moles of total Pd or surface-exposed Pd in the catalyst specimen, as appropriate. In the case of the reaction using $Pd/(YZrLaGdHf)_xO_2$, the specimen was treated with H_2 at 100 °C prior to catalytic experiment. After the reaction, the catalyst was recovered by centrifugation, washed twice with water and ethanol, then redispersed in aqueous solution and used for repeated tests under the same conditions. Since the catalyst cannot be completely recovered, the same reaction was carried out twice, and the recovered catalyst was combined and used in the next reaction.

2.5. Characterization: Powder XRD patterns were recorded using a Rigaku Ultima IV diffractometer with Cu K_α radiation (λ = 1.54056 Å). Nitrogen adsorption-desorption isotherms were acquired at −196 °C using a BELSORP-max system (MicrotracBEL Corp.). Samples were degassed at 150 °C for 3 h under vacuum to remove physisorbed water prior to each trial. Specific surface areas were calculated using the BET method based on the nitrogen adsorption data. Metal concentrations in the samples were determined using ICP-AES, employing a Nippon Jarrell-Ash ICAP-575 Mark II instrument. STEM images and elemental maps were obtained with a JEOL-ARM 200F apparatus equipped with a Kvex energy-dispersive X-ray detector (JED-2300T) operating at 200 kV. CO pulse adsorption analyses were performed using a BEL-

METAL-1 instrument (BEL Japan, Inc.) as a means of assessing the extent of Pd dispersion. Each sample was pretreated under a flow of He at 50 °C for 15 min and subsequently under a H_2 flow at 50 °C for 60 min. The CO adsorption of each specimen was assessed at 323 K under a flow of 1% CO in He at a rate of 20 ml·min^{-1}. Pd K-edge X-ray absorption fine structure (XAFS) spectra were obtained in the transmission mode using the BL01B1 beamline at the SPring-8 facility operated by JASRI in Harima, Japan (proposal numbers 2023A1668 and 2023B1805), using a Si(111) monochromator. In preparation for these analyses, each sample was formed into a pellet and held in a batch-type in situ XAFS cell. During reduction sequences, the sample was reduced under a 45 mL/min flow of a mixture comprising 33% H_2 in He while heating at a rate of 10 °C/min to a constant temperature. The H_2-D_2 exchange reaction was monitored using a BELCATII system (MicrotracBEL Corp.). After pretreatment under a He flow at 323 K for 30 min, the H_2-D_2 exchange reaction was performed at 50 °C using 25% H_2 in He or 25% D_2 in He at a flow rate of 25 ml·min^{-1}. The products of this process (H_2, HD and D_2) were analyzed using an online mass spectrometer and the rate constant was determined based on the quantity of HD (m/z =3) that was generated.

2.6. In situ ETEM

The thermal stability of each specimen was ascertained using an ETEM apparatus (Titan ETEM G2, Thermo Fisher Scientific Inc., USA) employing a Cs corrector in conjunction with the objective lens together with a monochromator and a K3-IS Direct Detection camera (Gatan, Inc., USA). The accelerating voltage and electron current flux were set at 300 kV and less than 4 A/cm^2, respectively, and observations under these conditions did not cause serious damage to the HEO support. The material was heated from room temperature to 700 °C under H_2 of 100 Pa at a heating rate of 5 °C/min using a NanoEx/i-v device (Thermo Fisher Scientific Inc., USA).

2.7. DFT calculations. First-principles calculations were conducted using the projector augmented-wave method[24] as implemented in the VASP code.[25-26] The Perdew-Burke-Ernzerhof functional as tuned for solids (PBEsol)[27] was employed. A surface cation was changed to Pd. The La_2O_3 slab model used in a previous study by the authors[28] was also used, in which a Hubbard U[29] based on the relationship U-J = 3 eV was added to the valence 5d states of La in La_2O_3. The calculated model is $La_{71}PdO_{108}$. The experimentally determined lattice parameter a=5.28825Å for a standard fluorite cell was used to construct the HEO model for $Y_{13}Zr_{13}La_{13}Gs_{12}Hf_{12}PdO_{128}$ per supercell. The Pd site in this model were fixed at the outermost surface of the model, and elements were randomly distributed at the remaining cation sites. The (100) termination of the fluorite structure had a nonpolar type C morphology based on the definition proposed by Hinuma.[30] Half of the atoms in the outermost layers, which comprised cations, were removed in a striped pattern to obtain a slab that was nonpolar when all cations were the same.[31] All internal coordinates were relaxed and

the atom positions were allowed to fully relax. Spin polarization was considered. Additionally, a Pd_{96} model was considered.

Calculations with HCO_3^- adsorbed on the slab with negative charge could not be performed in conjunction with three-dimensional periodic boundary conditions. Therefore, neutral HCO_3 was adsorbed. The electronic density of states (DOS) was obtained for HCO_3 on HEO, HEO, HCO_3 on La_2O_3, La_2O_3, HCO_3 on Pd, and Pd, respectively. The DOS for all atoms in the model, partial dos for the Pd atom, and O in HCO_3 that is adsorbed to Pd are shown in the figure. There are two Pd-O bonds for HCO_3 adsorbed to Pd, and DOS for the Pd-O pair where O does not bond to H is shown.

3. Results & Discussion

3.1. Synthesis and Characterization of Pd-based HEO samples

Scheme 1 shows the illustration of the synthesis of Pd@$(YZrLaGdHf)_xO_2$ and Pd/$(YZrLaGdHf)_xO_2$. A specimen of the HEO incorporating 1.0 wt% Pd (Pd@$(YZrLaGdHf)_xO_2$) was synthesized using a solution-based hydrothermal method involving all dissolved metal salts in the presence of P123 as surfactant and hexamethylenetetramine as a precipitant.[32] This was followed by calcination in air at 400, 600 or 800 °C for 2 h. Pd@$(TiZrLaCeHf)_xO_2$ was prepared by the same procedure but using Ti and Ce precursors instead of precursors containing Y and Gd. $(YZrLaGdHf)_xO_2$ and $(TiZrLaCeHf)_xO_2$ were also prepared using the same process but without the Pd precursor with subsequent calcination in air at 800 °C for 2 h. For comparison purposes, HEO specimens supporting 1.0 wt% Pd (Pd/$(YZrLaGdHf)_xO_2$ and Pd/$(TiZrLaCeHf)_xO_2$) were prepared by the conventional impregnation method followed by reduction at 400 °C under H_2.

Figure S1a presents the X-ray diffraction (XRD) patterns obtained from the $(YZrLaGdHf)_xO_2$-based specimens. The Pd@$(YZrLaGdHf)_xO_2$ and Pd/$(YZrLaGdHf)_xO_2$ calcined at 800 °C were both confirmed to have fluorite structures, suggesting that low levels of Pd did not change the HEO structure.[33] In contrast, the samples calcined at 400 °C generated various broad peaks but not the characteristic peaks assignable to a fluorite structure (**Figure S1b**). These data indicated that single-phase HEO materials were not formed by the calcination at 400 °C. The N_2 adsorption/desorption isotherms of these same two specimens both exhibited hysteresis indicative of a mesoporous structure whereas this structure was evidently collapsed by the following treatment at 800 °C (**Figure S1c**). In addition, the Brunauer–Emmett–Teller (BET) surface area (S_{BET}) decreased significantly upon increasing the calcination temperature, from 83 $m^2\ g^{-1}$ at 400 °C to 6 $m^2\ g^{-1}$ at 800 °C (**Table S1**). In the XRD pattern of the $(TiZrLaCeHf)_xO_2$-based specimens, the peaks due to a fluorite structure were intensified with increasing the calcination temperature, but the patterns calcined at 800 °C show the appearance of additional peaks (**Figure S2a** and **b**). Similar trends can be observed with regard

to the N_2 adsorption/desorption data obtained from these $(TiZrLaCeHf)_xO_2$-based specimens compared with $(YZrLaGdHf)_xO_2$-based ones (**Figure S2c**).

In situ X-ray absorption fine structure (XAFS) analyses were conducted to elucidate the stability of the Pd species under an H_2 atmosphere at elevated temperatures. The shape of the Pd K-edge X-ray absorption near-edge structure (XANES) spectrum of Pd@$(YZrLaGdHf)_xO_2$ before reduction resembled that of PdO but differed from that of Pd foil and contained two distinct peaks attributed to the allowed 1s–5p transition (**Figure 1a**). The spectrum acquired at 600 °C under an H_2 atmosphere resembled that of the material prior to reduction and that of PdO. However, a more detailed inspection found an adsorption edge position of 24,348 eV, similar to that of Pd foil but lower than the values of the material before reduction and of PdO. This outcome provided evidence that the valence state of Pd in the Pd@$(TiZrLaCeHf)_xO_2$ at 600 °C under H_2 was between 0 and +2 (**Figure S3**).

The Fourier-transform extended X-ray absorption fine structure (FT-EXAFS) spectrum of the Pd@$(YZrLaGdHf)_xO_2$ before reduction contained a peak attributed to Pd–O bonds and peaks due to Pd–O–Pd and/or Pd–O–M (M= Y, Zr, La, Gd, Hf) bonds at approximately 1.6 and 3.0 Å, respectively (**Figure 1b**). The intensity of the latter peaks relative to that of the former peak gradually decreased with increases in the reduction temperature. A small peak related to contiguous Pd–Pd bonds was also evident. Wavelet-transformed EXAFS (WT-EXAFS) is a useful tool for identifying the nature of surrounding atoms not only on the basis of interatomic distance but also backscattering amplitude.[34] The WT-EXAFS spectrum obtained from the Pd@$(YZrLaGdHf)_xO_2$ before reduction contained peaks attributable to Pd–O bonds and to Pd–O–Pd and/or Pd–O–M (M= Y, Zr, La, Gd, Hf) bonds (**Figure 1e**), consistent with the PdO reference (**Figure S4a**). The Pd@$(YZrLaGdHf)_xO_2$ heated at 600 °C under H_2 generated a main peak due to Pd–O bonds with an R value of 1.5 Å and a k of 5.0 cm^{-1}, but the peaks related to Pd–O–Pd and/or Pd–O–M bonds were small (**Figure 1c**). In addition, a new and less intense peak appeared with an R of 2.5 Å and k of 11.0 cm^{-1}. This peak clearly differed from that related to the Pd–Pd bonds in Pd foil (R = 2.5 Å and k = 9.1 cm^{-1}) (**Figure S4b**), suggesting an interaction between heavier elements such as La, Gd and Hf rather than with Pd.

Scanning transmission electron microscopy (STEM) images of the Pd@$(YZrLaGdHf)_xO_2$ before reduction did not show any noticeable particles. In addition, an EDX analysis demonstrated the uniform distributions of Y, Zr, La Gd, and Hf throughout the matrix but partial aggregation of the Pd (**Figure S5**). These results are in agreement with the XAFS data and so it appears that Pd was present in the form of partially aggregated oxides within the HEO matrix. Notably, no nanoparticles were identified in STEM images even after reduction at 600 °C under H_2 (**Figure 2**). EDX mapping also confirmed the homogeneous distribution of all elements in this material, with good dispersion of Pd and an absence of aggregation. These findings demonstrated that partially aggregated Pd oxides were transformed into isolated entropy-

stabilized particles as suggested by the XAFS analysis. It is therefore evident that a homogeneous solid-solution phase composed of multiple elements was synthesized (**Figures 1d** and **f**).

Pd species supported on the $(YZrLaGdHf)_xO_2$ were found to undergo rapid reduction. As such, the Pd K-edge in situ XANES spectrum of the Pd/$(YZrLaGdHf)_xO_2$ following reduction at 50 °C was similar to that of Pd foil (**Figure 3a**). In addition, the FT-EXAFS spectrum exhibited a single intense peak associated with Pd–Pd bonds at 2.5 Å even at 50 °C (**Figure 3b**). The WT-EXAFS spectrum acquired from the Pd/$(YZrLaGdHf)_xO_2$ after reduction at 100 °C exhibited a peak attributed to Pd–Pd bonds with an *R* of 2.5 Å and *k* of 8.5 cm^{-1} (**Figure 3c**). This peak was consistent with that generated by Pd foil (**Figure S4b**), suggesting the formation of Pd nanoparticles. STEM images showed nanoparticles having diameters in the range of 2 to 5 nm on the periphery of the HEA support after reduction at 100 °C (**Figure 4**). EDX mapping also confirmed the formation of aggregated Pd species. These results revealed that the impregnated Pd precursor is easily converted to Pd nanoparticles without benefiting from the stabilizing effect of HEO (**Figures 3d** and **f**).

In the case of the Pd@$(TiZrLaCeHf)_xO_2$, the shape of the XANES spectrum gradually changed beginning at 100 °C and was completely transformed into Pd metal at 200 °C (**Figure S6a**). In the FT-EXAFS spectrum, the intensities of the peaks related to Pd–O bonds at 1.5 Å and to Pd–O–Pd and/or Pd–O–M (M= Ti, Zr, La, Ce, Hf) bonds at 3.0 Å gradually decreased, while the peak ascribed to Pd–Pd bonds become stronger (**Figure S6b**). WT-EXAFS spectra confirmed the transformation of partially aggregated Pd oxide species into Pd nanoparticles by reduction at 200 °C (**Figures S6c-f**). Pd K-edge XAFS results suggest that the stability of the Pd species follows in the order of Pd/$(YZrLaGdHf)_xO_2$ < Pd@$(TiZrLaCeHf)_xO_2$ < Pd@$(YZrLaGdHf)_xO_2$. The relatively rapid reduction of incorporated Pd species within the $(TiZrLaCeHf)_xO_2$ compared with that within the $(YZrLaGdHf)_xO_2$ indicated that the entropy-stabilization effect was greatly affected by the composition of the HEO.[35-36]

The thermal stability of the Pd species in response to sintering under H_2 was further evaluated based on in situ ETEM observations at elevated temperatures under H_2 of 100 Pa. Interestingly, almost no change was observed with increases in temperature in trials with the Pd@$(YZrLaGdHf)_xO_2$ even at 600 °C, although very small nanoclusters/nanoparticles appeared above this temperature (**Figure 5a**). However, this behavior was rare because nanoparticle formation was confirmed at only nine observation points out of approximately 90 points in a 50 nm square region after heating under H_2 at 700 °C. These results clearly demonstrate that the Pd species encapsulated within the $(YZrLaGdHf)_xO_2$ exhibited high thermal stability and structural resistance to deterioration because of the high configurational entropy effect. In contrast, the impregnated Pd species on the $(YZrLaGdHf)_xO_2$ were readily reduced under the present conditions and the formation of nanoclusters/nanoparticles could be observed even at 100 to 200 °C (**Figure 5b**), consistent with the in situ XAFS results.

3.2. Catalytic performances in CO_2 hydrogenation into FA

The catalytic activities of these materials during CO_2 hydrogenation to FA were examined with the results shown in **Figure 6a**. A typical reaction was carried out in a basic aqueous solution containing 1.0 M $NaHCO_3$ under a total pressure of 2.0 MPa (H_2:CO_2 = 1:1) at 100 °C over a span of 6 h. To calculate TON values based on the quantities of surface exposed Pd, the dispersion of Pd species in each specimen was determined by pulsed CO adsorption measurements (**Table S2**).[37] The Pd@$(YZrLaGdHf)_xO_2$ exhibited the highest TON value of 5000 together with >99% selectivity. This performance was more than eight times higher than that of the Pd/$(YZrLaGdHf)_xO_2$. It should also be noted that no reaction byproducts were found in either the liquid or gas phase. Presumably, the lack of Pd aggregation, as evidenced by the in situ XAFS and TEM analyses, resulted in high activity per surface Pd despite the small amount of Pd available for the reaction. The recovered catalyst could also be reused at least three times without any loss of activity (**Figure S7**). The effectiveness of the incorporation of Pd within the HEO matrix was also demonstrated based on a comparison between the Pd@$(TiZrLaCeHf)_xO_2$ and Pd/$(TiZrLaCeHf)_xO_2$. The activity of the Pd@$(TiZrLaCeHf)_xO_2$ was found to be superior to Pd/$(YZrLaGdHf)_xO_2$, but was inferior to that of the Pd@$(YZrLaGdHf)_xO_2$. This finding can also be explained by the in situ XAFS results, in which the Pd species in the Pd@$(TiZrLaCeHf)_xO_2$ underwent reduction at lower temperatures compared with those in the Pd@$(YZrLaGdHf)_xO_2$, but at higher temperatures compared with those in the Pd/$(YZrLaGdHf)_xO_2$.

To further assess the advantages of HEO materials, the catalytic activity of the Pd@$(YZrLaGdHf)_xO_2$ was compared with those of single metal oxides containing Pd species prepared by a similar hydrothermal method. These results are also included in **Figure 6a**. The TON values obtained using the Pd@Y_xO_y, Pd@Zr_xO_y, Pd@La_xO_y, Pd@Gd_xO_y and Pd@Y_xO_y specimens were all lower than that for the Pd@$(YZrLaGdHf)_xO_2$. A similar trend was observed upon comparing the Pd@$(TiZrLaCeHf)_xO_2$ and single metal oxides made of the same components, although the Pd@Zr_xO_y showed higher activity than that of the Pd@$(TiZrLaCeHf)_xO_2$ (**Figure S8**). Moreover, the catalytic activities of the Pd@$(TiZrLaCeHf)_xO_2$ samples prepared by calcination at 400 and 600 °C, which produced XRD patterns having broad peaks without characteristic peaks assignable to the fluorite structure, were substantially lower than those of Pd@$(TiZrLaCeHf)_xO_2$ samples calcined at 800 °C (**Figure S9**). This occurred despite the lower BET surface area of the latter (**Table S1**). From these data, it is apparent that the incorporation of Pd species within the oxide matrix and entropy-driven stabilization provided by the single-phase HEO were required to obtain high activity during CO_2 hydrogenation.

Based on previous studies, a possible reaction mechanism for CO_2 hydrogenation to FA over metal catalysts can be proposed.[38-41] In this process, the dissociation of H_2 on Pd yields a metal hydride species (***step 1***), followed by the adsorption of a HCO_3^- ion formed from the reaction of dissolved CO_2 in the basic aqueous solution (***step 2***). Next, dissociated active H atoms attack the C atom of the adsorbed HCO_3^- to afford a formate intermediate (***step 3***). Finally, the O atom of the OH group undergoes attack by another H

atom (***step 4***), leading to the production of formate and H_2O (***step 5***), accompanied by regeneration of the initial active species. When HCO_3^- was used as a sole carbon source without gaseous CO_2, the catalytic activity significantly decreased. Additionally, in the previous investigation using $PdAg/TiO_2$ catalyst, the use of $^{13}CO_2$ in D_2O as a solvent (with 0.5 M NaOH) generated a sole peak at 170.8 ppm due to the deprotonated $H^{13}COO^-$ by ^{13}C NMR spectroscopy without the formation of byproducts.[20] These experiments provide firm evidence that the FA originates from CO_2. An analysis of the effect of H_2 pressure was performed and the Pd-incorporated $Pd@(YZrLaGdHf)_xO_2$ catalysts displayed a lower reaction order (0.25) compared with the Pd-supported $Pd/(YZrLaGdHf)_xO_2$ (0.33) (**Figure 6b)**. In the case of the H-D exchange reaction ($H_2 + D_2 \leftrightarrow 2HD$), the HD formation rate (m/z =3) based on the surface exposed Pd species was significantly enhanced when using the $Pd@(YZrLaGdHf)_xO_2$ compared with the $Pd/(YZrLaGdHf)_xO_2$ by a factor of more than four (**Figure S10**). These findings indicate that the dissociation of H_2 occurred more easily on the Pd- incorporated $Pd@(YZrLaGdHf)_xO_2$ than on the Pd-supported $Pd/(YZrLaGdHf)_xO_2$. Additionally, the $Pd@(YZrLaGdHf)_xO_2$ catalysts exhibited lower reaction order values than the $Pd/(YZrLaGdHf)_xO_2$ in trials assessing the effect of HCO_3^- concentration, as determined using the slope obtained at low HCO_3^- concentrations (**Figure 6c**).

Density of states (DOS) calculations were performed to confirm the bonding state between HCO_3 and Pd on the surface of HEO (100) ($Y_{13}Zr_{13}La_{13}Gs_{12}Hf_{12}Pd_1O_{128}$), La_2O_3 (100) ($La_{71}Pd_1O_{108}$), and Pd metal (111) (**Figure 7**). The DOS of Pd substituting a surface cation in HEO and La_2O_3 strongly depends on the substrate. There is a strong bonding state just above the Fermi level between a Pd atom at the surface of HEO and O in HCO_3 adsorbed to this Pd. The HCO_3 is adsorbed as a neutral species due to computational constraints. Adding an extra electron fills this state, resulting in a chemical bond between Pd and HCO_3. On the other hand, there is no such bonding state for HCO_3 and Pd on the surface of La_2O_3 or Pd metal slab surface, suggesting enhanced reactivity of HCO_3 with HEO compared to La_2O_3 and Pd metal.

Further DFT calculations showed that the adsorption energy (E_{ad}) of the HCO_3^- ion in ***step 2*** on a Pd atom in the HEO (100) ($Y_{13}Zr_{13}La_{13}Gs_{12}Hf_{12}Pd_1O_{128}$) was −2.63eV (**Figure S11**). This value is higher than that of –2.58 eV determined for La_2O_3 (100) ($La_{71}Pd_1O_{108}$), suggesting that the HEO should be more reactive than La_2O_3 with regard to HCO_3^- adsorption. These kinetics evaluations and calculation results indicate that the rate determining (***step 3***) will be promoted by entropy-stabilized Pd species.

Conclusion

In summary, we synthesized $(YZrLaGdHf)_xO_2$ incorporating Pd based on an entropy-driven strategy using a liquid phase reaction. The structure of the as-synthesized $Pd@(YZrLaGdHf)_xO_2$ was confirmed the presence of partially segregated Pd oxides along with the homogeneous distribution of metal oxides based

on five elements. *In situ* observations at elevated temperatures under H_2 established the formation of entropy-stabilized isolated Pd species at 600 °C, providing evidence that thermal stability was enhanced by the increased configurational entropy of this multi-element material. In contrast, Pd species loaded onto the $(YZrLaGdHf)_xO_2$ surface readily agglomerated in the temperature range of 100 to 200 °C. The Pd@$(YZrLaGdHf)_xO_2$) showed higher activity in the hydrogenation of CO_2 to FA compared with the Pd/$(YZrLaGdHf)_xO_2$. Kinetics data and DFT calculations indicated that the presence of entropy-stabilized Pd species promoted H_2 dissociation together with the attack of dissociated H atoms on C atoms in HCO_3^- ions. The techniques reported herein could allow the development of environmentally friendly hydrogen storage systems mediated by CO_2 and FA.

ASSOCIATED CONTENT

Supporting Information

Supporting Information is available free of charge via the Internet at http://pubs.acs.org. Experimental details (characterization, In situ ETEM, and DFT calculation), additional data for XRD, N_2-adsorption/desorption, XAFS, WT-EXAFS, STEM, EDX, CO adsorption, H-D exchange reaction.

AUTHOR INFORMATION

Corresponding Authors

Kohsuke Mori; Division of Materials and Manufacturing Science, Graduate School of Engineering, Osaka University, 2-1 Yamada-oka, Osaka 565-0871, Japan; Innovative Catalysis Science Division, Institute for Open and Transdisciplinary Research Initiatives (ICS-OTRI), Osaka University, Suita, Osaka 565-0871, Japan.
orcid.org/0000-0003-3915-4528
E-mail: mori@mat.eng.osaka-u.ac.jp

Authors

Yuki Shimada; Division of Materials and Manufacturing Science, Graduate School of Engineering, Osaka University, 2-1 Yamada-oka, Osaka 565-0871
Hideto Yoshida; SANKEN, Osaka University, 8-1Mihogaoka, Ibaraki, Osaka 567-0047, Japan.
Yoyo Hinuma; Department of Energy and Environment, National Institute of Advanced Industrial Science and Technology (AIST), 1-8-31, Midorigaoka, Ikeda, Osaka 563-8577, Japan
Hiromi Yamashita; Division of Materials and Manufacturing Science, Graduate School of Engineering, Osaka University, 2-1 Yamada-oka, Osaka 565-0871; Innovative Catalysis Science Division, Institute for Open and Transdisciplinary Research Initiatives (ICS-OTRI), Osaka University, Suita, Osaka 565-0871, Japan.

Author Contributions

K.M. supervised the project and wrote the manuscript. Y.S. performed the catalyst preparation, characterization, and catalytic reactions. H.Y. performed the TEM observation. Y. H performed the DFT calculation. H.Y. helped supervise the project. The manuscript was written through discussion with all authors. All authors have given approval to the final version of the manuscript.

Notes

The authors declare no competing financial interest.

Acknowledgement

This work was financially supported by Grants-in-Aid for Scientific Research (A24H003950, T22K189200, JP23K21080, JP24H02205) from the Japan Society for the Promotion of Science (JSPS). Part of this work was supported by Yazaki Memorial Foundation for Science and Technology. Part of TEM experiment was carried out by using a facility in the Research Center for Ultra-High Voltage Electron Microscopy, Osaka University. The synchrotron radiation experiments for XAFS measurements were performed at the BL01B1 beamline in SPring-8 with the approval from JASRI (2023A1668 and 2023B1805).

References

1. George, E. P.; Raabe, D.; Ritchie, R. O., High-Entropy Alloys. *Nat. Rev. Mater.* **2019,** *4*, 515-534.
2. Miracle, D. B.; Senkov, O. N., A Critical Review of High Entropy Alloys and Related Concepts. *Acta Mater.* **2017,** *122*, 448-511.
3. Hashimoto, N.; Mori, K.; Matsuzaki, S.; Iwama, K.; Kitaura, R.; Kamiuchi, N.; Yoshida, H.; Yamashita, H., Sub-nanometric High-Entropy Alloy Cluster: Hydrogen Spillover Driven Synthesis on CeO2 and Structural Reversibility. *JACS Au* **2023,** *3*, 2131-2143.
4. Mori, K.; Hashimoto, N.; Kamiuchi, N.; Yoshida, H.; Kobayashi, H.; Yamashita, H., Hydrogen Spillover-Driven Synthesis of High-Entropy Alloy Nanoparticles as a Robust Catalyst for CO_2 Hydrogenation. *Nat. Commun.* **2021,** *12*, 3884.
5. Rost, C. M.; Sachet, E.; Borman, T.; Moballegh, A.; Dickey, E. C.; Hou, D.; Jones, J. L.; Curtarolo, S.; Maria, J.-P., Entropy-stabilized Oxides. *Nat. Commun.* **2015,** *6*, 8485.
6. Oses, C.; Toher, C.; Curtarolo, S., High-entropy Ceramics. *Nat. Rev. Mater.* **2020,** *5*, 295-309.

7. Sarkar, A.; Wang, Q.; Schiele, A.; Chellali, M. R.; Bhattacharya, S. S.; Wang, D.; Brezesinski, T.; Hahn, H.; Velasco, L.; Breitung, B., High-Entropy Oxides: Fundamental Aspects and Electrochemical Properties. *Adv. Mater.* **2019,** *31*, 1806236.
8. Sarkar, A.; Velasco, L.; Wang, D.; Wang, Q.; Talasila, G.; de Biasi, L.; Kübel, C.; Brezesinski, T.; Bhattacharya, S. S.; Hahn, H.; Breitung, B., High Entropy Oxides for Reversible Energy Storage. *Nat. Commun.* **2018,** *9*, 3400.
9. Ma, Y.; Ma, Y.; Wang, Q.; Schweidler, S.; Botros, M.; Fu, T.; Hahn, H.; Brezesinski, T.; Breitung, B., High-entropy Energy Materials: Challenges and New Opportunities. *Energy Environ. Sci.* **2021,** *14*, 2883-2905.
10. Xu, H.; Zhang, Z.; Liu, J.; Do-Thanh, C.-L.; Chen, H.; Xu, S.; Lin, Q.; Jiao, Y.; Wang, J.; Wang, Y.; Chen, Y.; Dai, S., Entropy-stabilized Single-atom Pd Catalysts via High-Entropy Fluorite Oxide Supports. *Nat. Commun.* **2020,** *11*, 3908.
11. Chen, H.; Sun, Y.; Yang, S.; Wang, H.; Dmowski, W.; Egami, T.; Dai, S., Self-regenerative Noble Metal Catalysts Supported on High-Entropy Oxides. *Chem. Commun.* **2020,** *56*, 15056-15059.
12. Mehrabi-Kalajahi, S.; Moghaddam, A. O.; Hadavimoghaddam, F.; Varfolomeev, M. A.; Zinnatullin, A. L.; Vakhitov, I.; Minnebaev, K. R.; Emelianov, D. A.; Uchaev, D.; Cabot, A.; Il'yasov, I. d. R.; Davletshin, R. R.; Trofimov, E.; Khasanova, N. M.; Vagizov, F. G., Entropy-stabilized Metal Oxide Nanoparticles Supported on Reduced Graphene Oxide as a Highly Active Heterogeneous Catalyst for SELECTIVe and Solvent-Free Oxidation of Toluene: a Combined Experimental and Numerical Investigation. *J. Mater. Chem. A* **2022,** *10*, 14488-14500.
13. Chen, H.; Fu, J.; Zhang, P.; Peng, H.; Abney, C. W.; Jie, K.; Liu, X.; Chi, M.; Dai, S., Entropy-stabilized Metal Oxide Solid Solutions as CO Oxidation Catalysts with High-Temperature Stability. *J. Mater. Chem. A* **2018,** *6*, 11129-11133.
14. Zhao, J.; Bao, J.; Yang, S.; Niu, Q.; Xie, R.; Zhang, Q.; Chen, M.; Zhang, P.; Dai, S., Exsolution–Dissolution of Supported Metals on High-Entropy $Co_3MnNiCuZnOx$: Toward Sintering-Resistant Catalysis. *ACS Catal.* **2021,** *11*, 12247-12257.
15. Elmutasim, O.; Hussien, A. G.; Sharan, A.; AlKhoori, S.; Vasiliades, M. A.; Taha, I. M. A.; Kim, S.; Harfouche, M.; Emwas, A.-H.; Anjum, D. H.; Efstathiou, A. M.; Yavuz, C. T.; Singh, N.; Polychronopoulou, K., Evolution of Oxygen Vacancy Sites in Ceria-Based High-Entropy Oxides and Their Role in N2 Activation. *ACS Appl. Mater. Interfaces* **2024,** *16*, 23038-23053.
16. Eppinger, J.; Huang, K.-W., Formic Acid As A Hydrogen Energy Carrier. *ACS Energy Lett.* **2017,** *2*, 188-195.
17. Jessop, P. G.; Ikariya, T.; Noyori, R., Homogeneous Hydrogenation of Carbon Dioxide. *Chem. Rev.* **1995,** *95*, 259-272.

18. Wang, W.; Wang, S.; Ma, X.; Gong, J., Recent Advances in Catalytic Hydrogenation of Carbon Dioxide. *Chem. Soc. Rev.* **2011,** *40*, 3703-3727.
19. Mellmann, D.; Sponholz, P.; Junge, H.; Beller, M., Formic Acid as a Hydrogen Storage Material - Development of Homogeneous Catalysts for Selective Hydrogen Release. *Chem. Soc. Rev.* **2016,** *45*, 3954-3988.
20. Mori, K.; Sano, T.; Kobayashi, H.; Yamashita, H., Surface Engineering of a Supported PdAg Catalyst for Hydrogenation of CO_2 to Formic Acid: Elucidating the Active Pd Atoms in Alloy Nanoparticles. *J. Am. Chem. Soc.* **2018,** *140*, 8902-8909.
21. Filonenko, G. A.; Vrijburg, W. L.; Hensen, E. J. M.; Pidko, E. A., On the Activity of Supported Au Catalysts in the Liquid Phase Hydrogenation of CO_2 to Formates. *J. Catal.* **2016,** *343*, 97-105.
22. Liu, M.; Xu, Y.; Meng, Y.; Wang, L.; Wang, H.; Huang, Y.; Onishi, N.; Wang, L.; Fan, Z.; Himeda, Y., Heterogeneous Catalysis for Carbon Dioxide Mediated Hydrogen Storage Technology Based on Formic Acid. *Adv. Energy Mater.* **2022,** *12*, 2200817.
23. Gunasekar, G. H.; Park, K.; Jung, K.-D.; Yoon, S., Recent Developments in the Catalytic Hydrogenation of CO_2 to Formic Acid/Formate using Heterogeneous Catalysts. *Inorg. Chem. Front.* **2016,** *3*, 882-895.
24. Blöchl, P. E., Projector augmented-wave method. *Phys. Rev. B* **1994,** *50*, 17953-17979.
25. Kresse, G.; Furthmüller, J., Efficient iterative schemes for ab initio total-energy calculations using a plane-wave basis set. *Phys. Rev. B* **1996,** *54*, 11169-11186.
26. Kresse, G.; Joubert, D., From ultrasoft pseudopotentials to the projector augmented-wave method. *Phys. Rev. B* **1999,** *59*, 1758-1775.
27. Perdew, J. P.; Ruzsinszky, A.; Csonka, G. I.; Vydrov, O. A.; Scuseria, G. E.; Constantin, L. A.; Zhou, X.; Burke, K., Restoring the Density-Gradient Expansion for Exchange in Solids and Surfaces. *Phys. Rev. Lett.* **2008,** *100*, 136406.
28. Hinuma, Y.; Toyao, T.; Kamachi, T.; Maeno, Z.; Takakusagi, S.; Furukawa, S.; Takigawa, I.; Shimizu, K.-i., Density Functional Theory Calculations of Oxygen Vacancy Formation and Subsequent Molecular Adsorption on Oxide Surfaces. *J. Phys. Chem. C* **2018,** *122*, 29435-29444.
29. Dudarev, S. L.; Botton, G. A.; Savrasov, S. Y.; Humphreys, C. J.; Sutton, A. P., Electron-energy-loss spectra and the structural stability of nickel oxide: An LSDA+U study. *Phys. Rev. B* **1998,** *57*, 1505-1509.
30. Hinuma, Y.; Kumagai, Y.; Oba, F.; Tanaka, I., Categorization of surface polarity from a crystallographic approach. *Comp. Mater. Sci.* **2016,** *113*, 221-230.
31. Hinuma, Y.; Kamachi, T.; Hamamoto, N., Auto-Generation of Corrugated Nonpolar Stoichiometric Slab Models. *Mater. Trans.* **2020,** *61*, 78-87.

32. Wang, D.; Liu, Z.; Du, S.; Zhang, Y.; Li, H.; Xiao, Z.; Chen, W.; Chen, R.; Wang, Y.; Zou, Y.; Wang, S., Low-temperature Synthesis of Small-Sized High-Entropy Oxides for Water Oxidation. *J. Mater. Chem. A* **2019,** *7*, 24211-24216.
33. Anandkumar, M.; Bhattacharya, S.; Deshpande, A. S., Low Temperature Synthesis and Characterization of Single Phase Multi-Component Fluorite Oxide Nanoparticle Sols. *RSC Adv.* **2019,** *9*, 26825-26830.
34. Filez, M.; Redekop, E. A.; Poelman, H.; Galvita, V. V.; Ramachandran, R. K.; Dendooven, J.; Detavernier, C.; Marin, G. B., Unravelling the Formation of Pt–Ga Alloyed Nanoparticles on Calcined Ga-Modified Hydrotalcites by in Situ XAS. *Chem. Mater.* **2014,** *26*, 5936-5949.
35. Albedwawi, S. H.; AlJaberi, A.; Haidemenopoulos, G. N.; Polychronopoulou, K., High Entropy Oxides-Exploring a Paradigm of Promising Catalysts: A Review. *Mater. Design* **2021,** *202*, 109534.
36. AlKetbi, M.; Polychronopoulou, K.; Abi Jaoude, M.; Vasiliades, M. A.; Sebastian, V.; Hinder, S. J.; Baker, M. A.; Zedan, A. F.; Efstathiou, A. M., Cu-Ce-La-Ox as Efficient CO Oxidation Catalysts: Effect of Cu Content. *Appl. Surf. Sci.* **2020,** *505*, 144474.
37. Mori, K.; Hata, H.; Yamashita, H., Interplay of Pd Ensemble Sites Induced by GaOx Modification in Boosting CO_2 Hydrogenation to Formic Acid. *Applied Catalysis B: Environ.* **2023,** *320*, 122022.
38. Masuda, S.; Mori, K.; Futamura, Y.; Yamashita, H., PdAg Nanoparticles Supported on Functionalized Mesoporous Carbon: Promotional Effect of Surface Amine Groups in Reversible Hydrogen Delivery/Storage Mediated by Formic Acid/CO_2. *ACS Catal.* **2018,** *8*, 2277-2285.
39. Mori, K.; Masuda, S.; Tanaka, H.; Yoshizawa, K.; Che, M.; Yamashita, H., Phenylamine-functionalized Mesoporous Silica Supported PdAg Nanoparticles: a Dual Heterogeneous Catalyst for Formic Acid/CO_2-mediated Chemical Hydrogen Delivery/Storage. *Chem. Commun.* **2017,** *53*, 4677.
40. Wiener, H.; Blum, J.; Feilchenfeld, H.; Sasson, Y.; Zalmanov, N., The Heterogeneous Catalytic Hydrogenation of Bicarbonate to Formate in Aqueous Solutions. *J. Catal.* **1988,** *110*, 184-190.
41. He, C.-S.; Gong, L.; Zhang, J.; He, P.-P.; Mu, Y., Highly Selective Hydrogenation of CO_2 into Formic Acid on a Nano-Ni Catalyst at Ambient Temperature: Process, Mechanisms and Catalyst Stability. *J. CO_2 Util.* **2017,** *19*, 157-164.

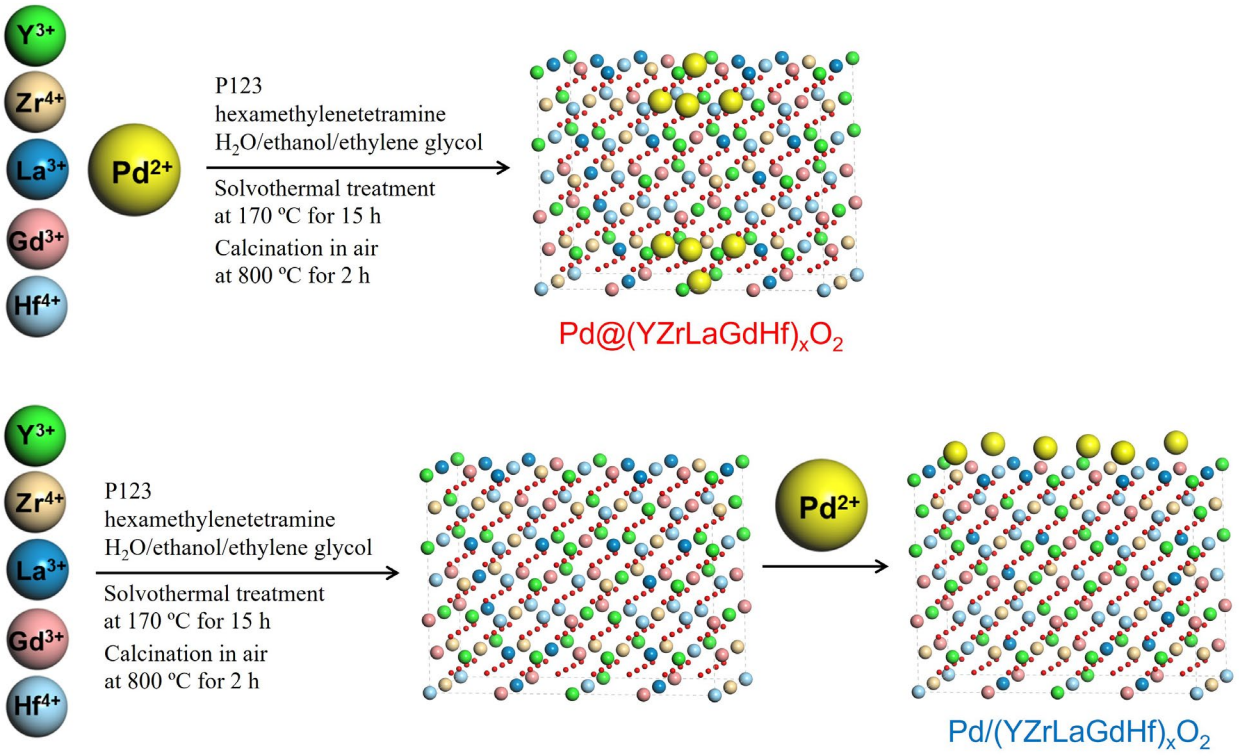

Scheme 1. Illustration of the synthesis of Pd@$(YZrLaGdHf)_xO_2$ and Pd/$(YZrLaGdHf)_xO_2$.

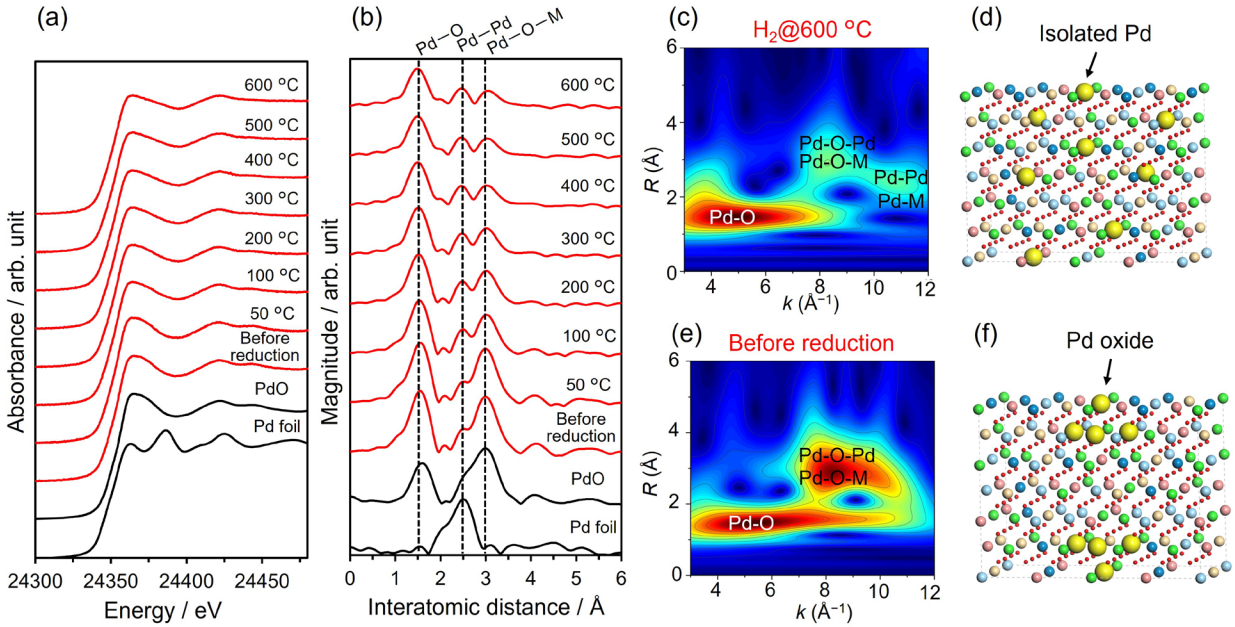

Figure 1 (a) Pd K-edge in situ XANES and (b) FT-EXAFS spectra acquired from the Pd@(YZrLaGdHf)$_x$O$_2$ under H_2 at elevated temperatures together with spectra for PdO and Pd foil as references. (c) WT-EXAFS spectra obtained after reduction at 600 ºC and (d) the proposed structure following this reduction. (e) WT-EXAFS spectra obtained prior to reduction and (f) the proposed structure before reduction.

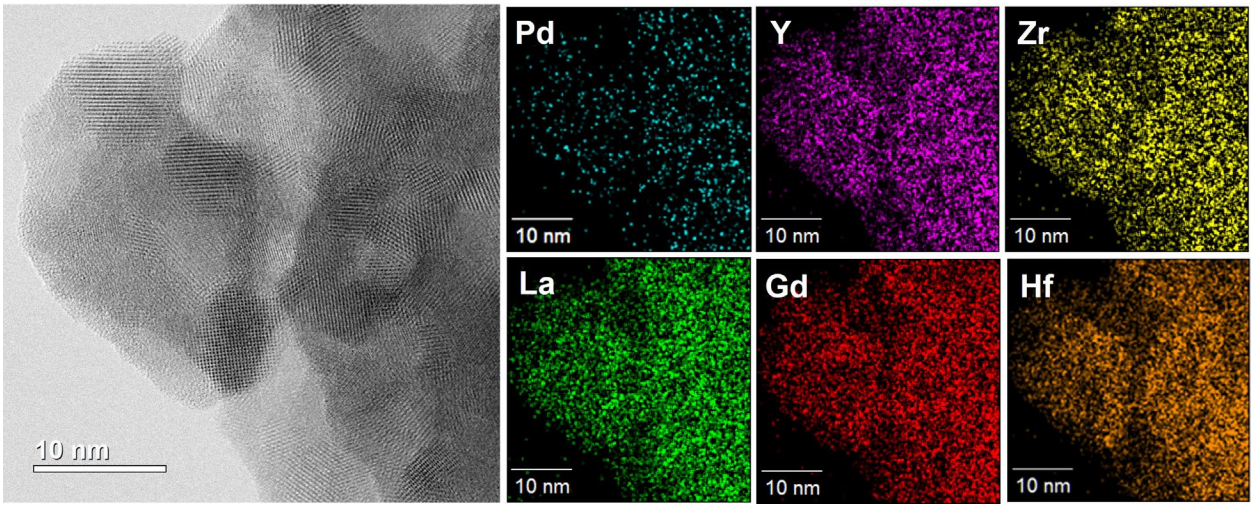

Figure 2. STEM image and EDX maps of the Pd@$(YZrLaGdHf)_xO_2$ after reduction at 600 ºC under H_2.

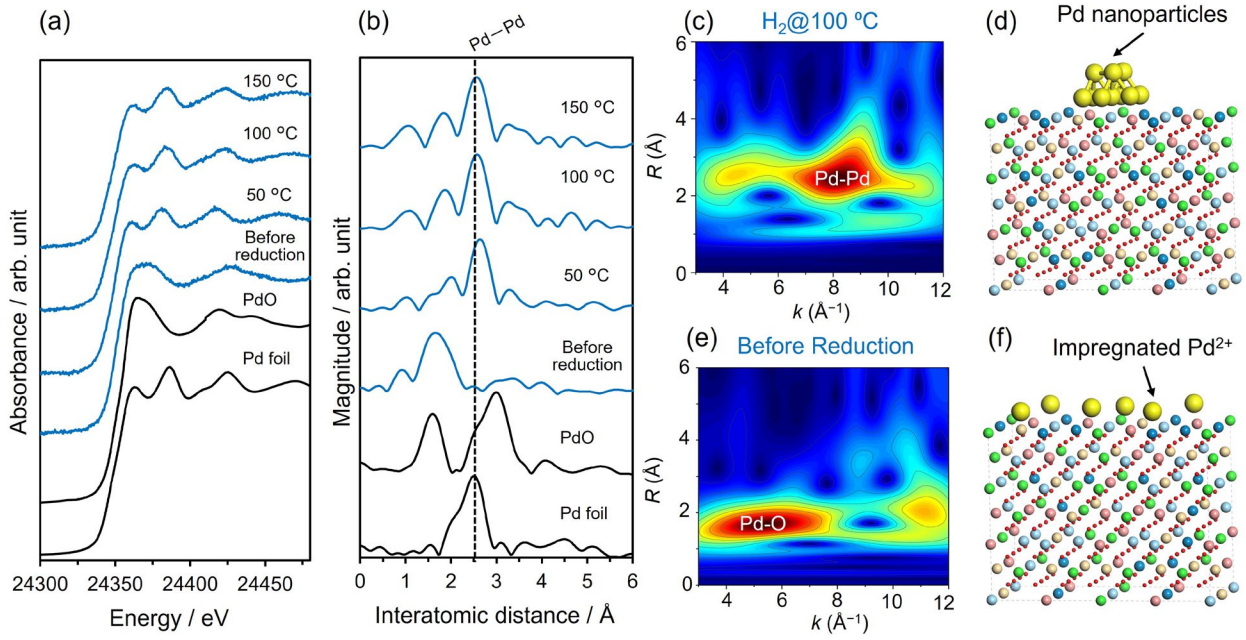

Figure 3 (a) Pd K-edge in situ XANES and (b) FT-EXAFS spectra acquired from the Pd/$(YZrLaGdHf)_xO_2$ under H_2 at elevated temperatures, together with data for PdO and Pd foil as references. (c) WT-EXAFS spectra obtained following reduction at 100 ºC and (d) the proposed structure after reduction. (e) WT-EXAFS spectra obtained before reduction and (f) the proposed structure before reduction.

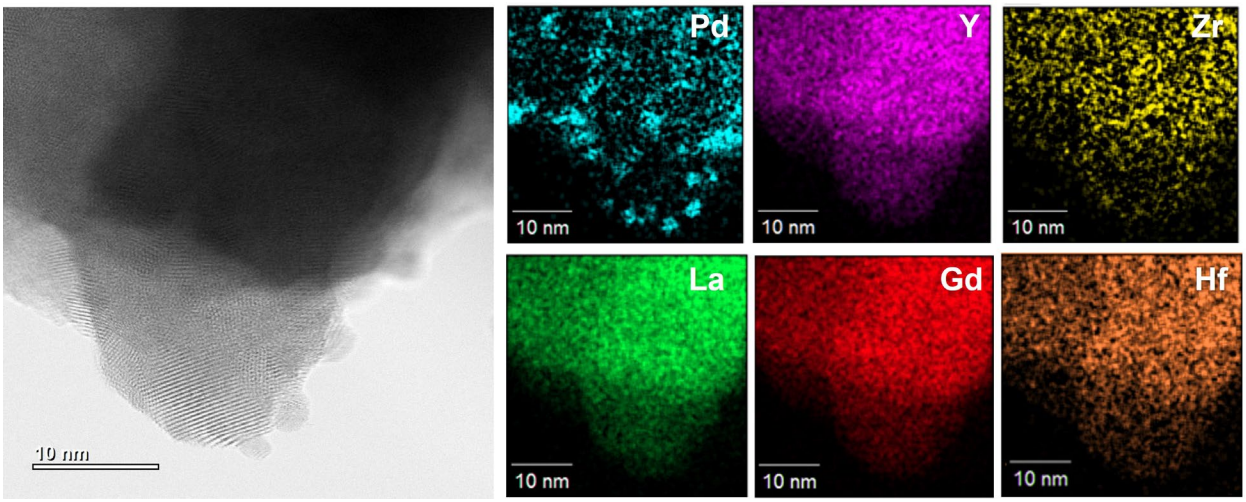

Figure 4. STEM image and EDX maps of the Pd/$(YZrLaGdHf)_xO_2$ after reduction at 100 ºC under H_2.

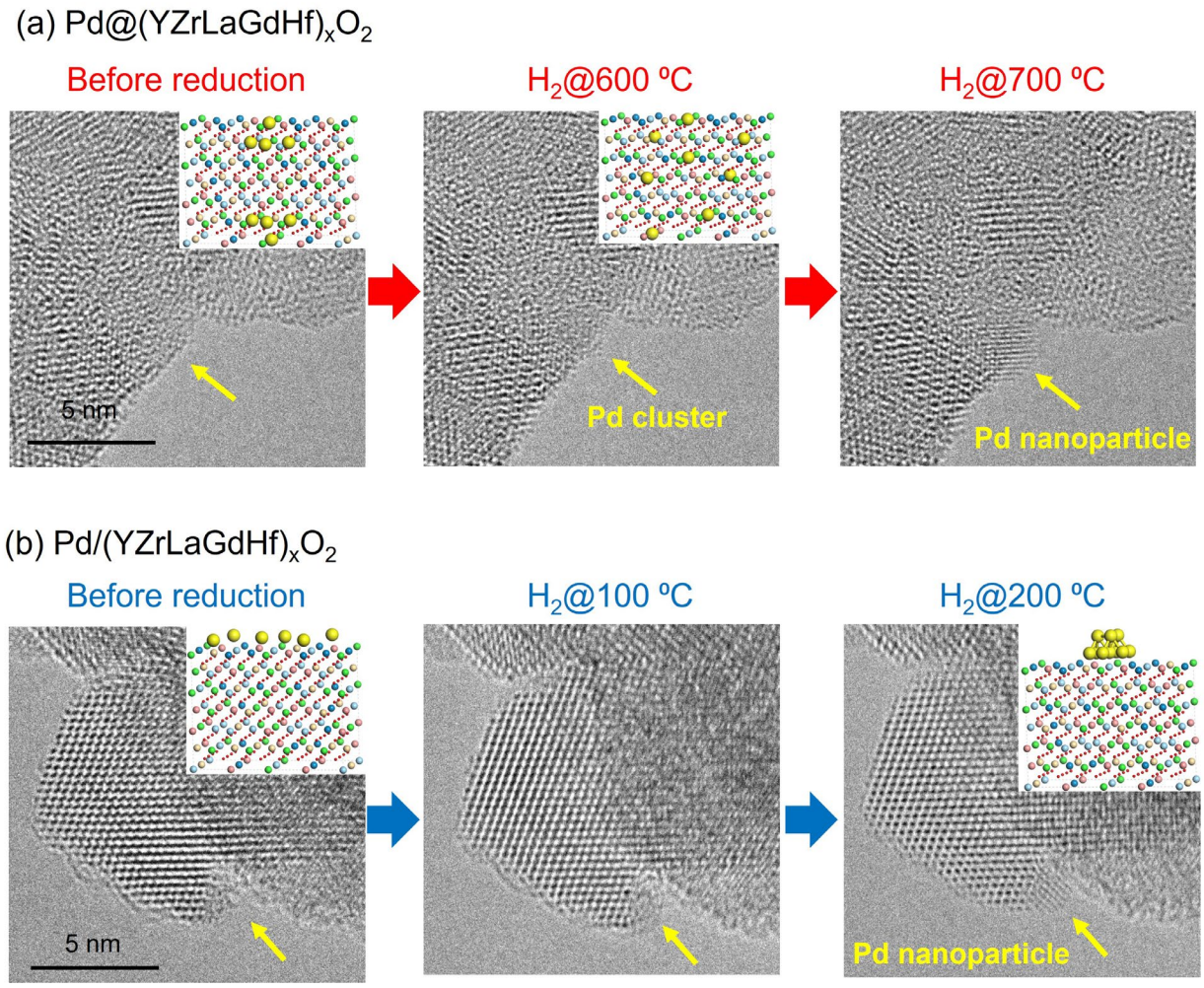

Figure 5. Representative in situ ETEM images of the (a) Pd@$(YZrLaGdHf)_xO_2$ and (b) Pd/$(YZrLaGdHf)_xO_2$.

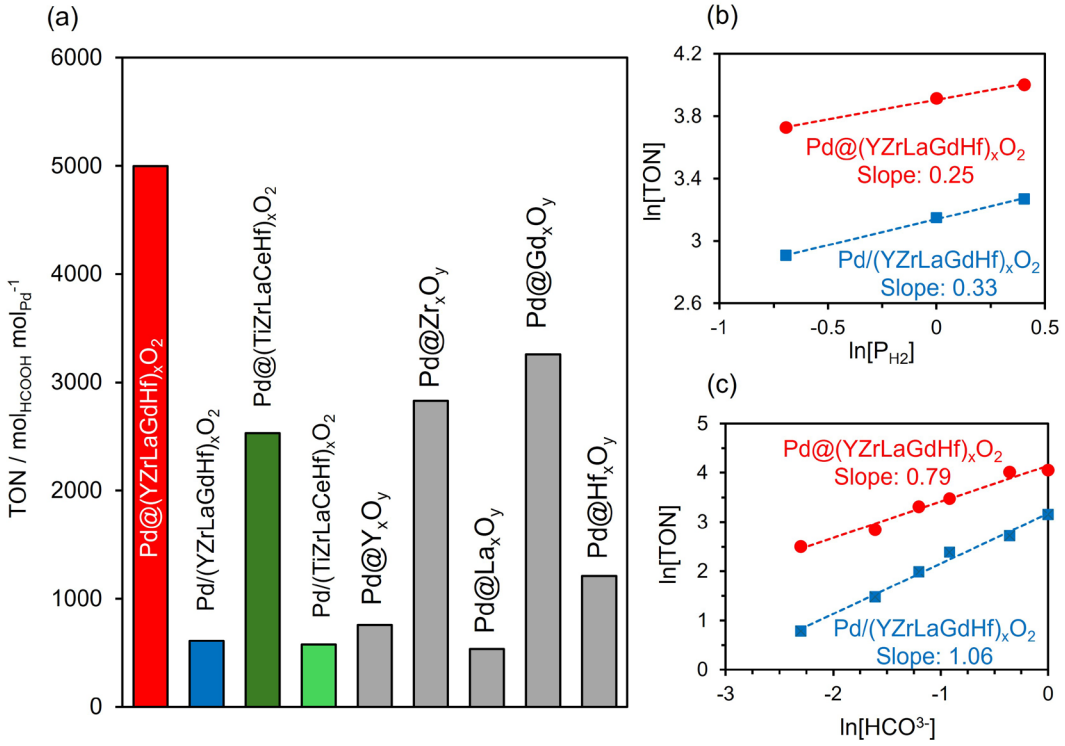

Figure 6. (a) TON values based on surface Pd atoms used to compare catalytic activities during CO_2 hydrogenation, (b) the effect of H_2 pressure on TON when using the Pd@(YZrLaGdHf)$_x$O$_2$ and Pd/(YZrLaGdHf)$_x$O$_2$, and (c) the effect of HCO_3^- concentration on TON when using the Pd@(YZrLaGdHf)$_x$O$_2$ and Pd/(YZrLaGdHf)$_x$O$_2$.

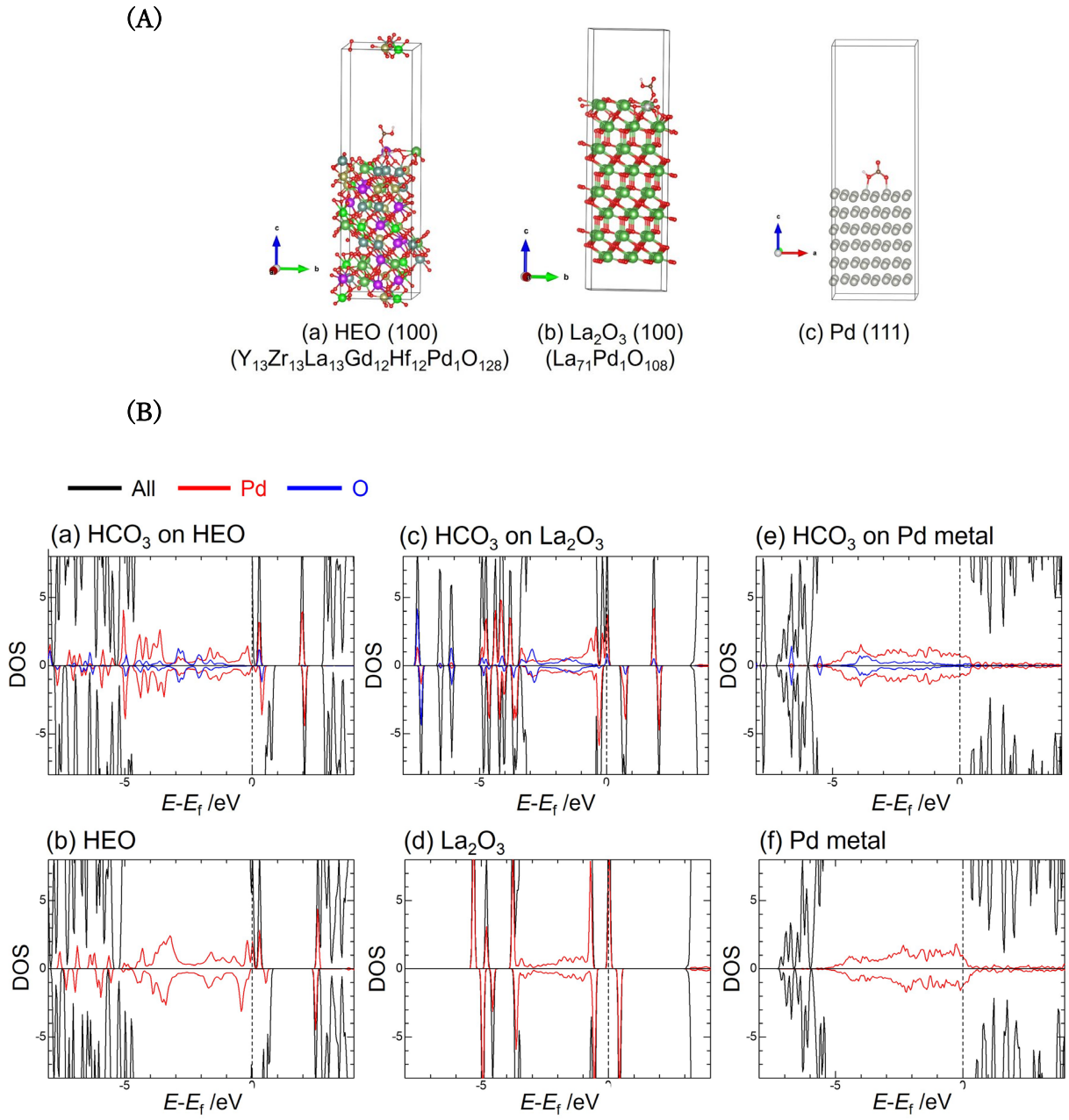

Figure 7. (A) Models for the (a) $Y_{13}Zr_{13}La_{13}Gd_{12}Hf_{12}Pd_1O_{128}$, (b) $La_{71}Pd_1O_{108}$, and (c) Pd slab containing HCO_3 used to obtain DOS based on DFT calculations. (B) The calculated DOS plots for (a) HCO_3 on HEO, (b) HEO, (c) HCO_3 on La_2O_3, (d) La_2O_3, (e) HCO_3 on Pd metal, and (f) Pd metal.

TOC Graphic

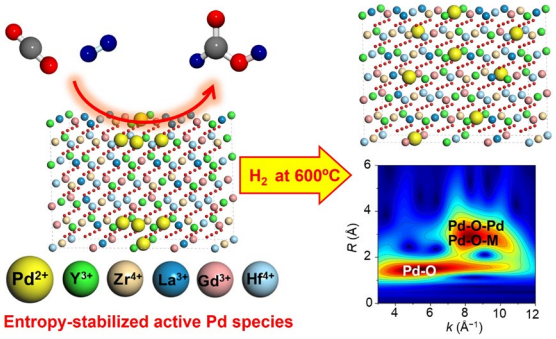
H2 at 600°C
Pd-O-Pd
Pd-O-M
Pd-O
R (Å)
k (Å⁻¹)
Pd2+
Y3+
Zr4+
La3+
Gd3+
Hf4+
Entropy-stabilized active Pd species